International Journal of Heat and Mass Transfer 246 (2025) 127036

Contents lists available at ScienceDirect

International Journal of Heat and Mass Transfer

journal homepage: www.elsevier.com/locate/hmt

Unsteady conjugate heat transfer effects on flow characteristics in transonic flow

Yann Dreze [*], Luca di Mare

Department of Engineering Science, Oxford University, Oxford Thermofluids Institute, Southwell Building, Oxford, OX20ES, United Kingdom

ARTICLE INFO

Keywords:
Conjugate heat transfer
Unsteady conjugate heat transfer
Thermal transients
Capacity measurement

ABSTRACT

We present a detailed study into compressible flows in presence of unsteady conjugate heat transfer to the walls. The investigation reveals that all flow quantities experience drift until thermal steady state is achieved in both fluid and solid domains. The drift follows a characteristic exponential decay, and we demonstrate that the heat transfer process between the two domains is ruled by the ratio of thermal capacity and the Stanton number that characterises the interface. To illustrate these effects, we numerically analyse the influence of slow thermal transients due to conjugate heat transfer on discharge characteristics of non-adiabatic nozzles. A transonic nozzle with thermally conducting walls is simulated using numerical methods with different fidelity, from one-dimensional reduced-order models to large eddy simulations, and the transient evolution of mass flow rate is monitored. Additionally, it is observed that while preheating does not affect the decaying time constant of the drift, the bounds of the decay are directly proportional to the initial temperature difference.

1. Introduction

Conjugate heat transfer (CHT), the thermal interaction between fluid flow and solid bodies, plays a crucial role in understanding and optimising the performance of many fluid dynamics domains. Its significance spans from microscopic levels, such as near-wall turbulence [1] or the use of nanofluids for improved heat transfer [2], to macroscale systems such as thermal management in spacecraft, insulation in nuclear reactors, cooling of turbine blades, and thermal regulation in battery technology, [3,4].

In turbomachinery, CHT is a critical aspect when designing the hot parts in high-pressure turbines [5,6]. This is particularly important when considering the increased inlet temperatures of next-generation aero-engines, which can exceed the melting points of current turbine blade materials. These components therefore require complex thermal cooling system and accurate thermal analysis is needed to ensure their longevity and safety.

1.1. Effects of steady conjugate heat transfer through the external walls on flow characteristics

The present work examines the transient impact of the external thermal boundary on non-isentropic internal flows. However, before looking at transient effects, let us first consider with an example the steady effects that external heat transfer can have on global flow characteristics.

A Rayleigh flow describes a frictionless, non-adiabatic flow through a constant area duct with heat transfer. Using isentropic relations, the dimensional mass flow rate in the duct is given by the following equation:

$$\dot{m} = \frac{A\,p_t}{\sqrt{T_t}}\sqrt{\frac{\gamma}{R}}\,M\left(1+\frac{\gamma-1}{2}M^2\right)^{-\frac{\gamma+1}{2(\gamma-1)}} \tag{1}$$

For the traditional Rayleigh flow setup, the inlet Mach number and stagnation temperature are fixed along with the outlet static pressure. Therefore, for a given entropy rise, the mass flow rate is proportional to the total pressure at the inlet.

The total pressure can be found using the outlet pressure and a closed-form solution for internal compressible flows with an arbitrary combination of area change, heat addition. Details of the implementation can be found in Appendix A. The development lead to Eq. (2) which is a second-order equation for the exit Mach number based on an inlet Mach number and a stagnation temperature ratio. This approach provides a tool for analysing the steady effects of heat transfer on flow characteristics in a quasi-one-dimensional setting.

$$\frac{\left(1+\frac{A_1}{A_2}+2\gamma M_1^2\right)}{\left(1+\frac{A_2}{A_1}+2\gamma M_2^2\right)}\sqrt{\frac{T_{t,1}\,f(M_2)}{T_{t,2}\,f(M_1)}}\,\frac{M_2}{M_1}-1=0 \tag{2}$$

When looking at the enthalpy-entropy diagram for a Rayleigh flow, on the subsonic branch the entropy change will lead to a change in total

---

[*] Corresponding author.
E-mail address: yann.dreze@engs.ox.ac.uk (Y. Dreze).

https://doi.org/10.1016/j.ijheatmasstransfer.2025.127036
Received 12 September 2024; Received in revised form 24 March 2025; Accepted 26 March 2025

Nomenclature

α	Thermal diffusivity
δ_f	Thermal boundary layer thickness
δ_s	Thermal penetration depth in the solid
$\dot{m}$	Mass flow rate
Γ	Capacity
γ	Ratio of specific heats
μ	Dynamic viscosity
ρ	Density
τ	Characteristic time
θ	Dimensionless temperature
ξ, ζ, η	Geodesic coordinates
A	Area
a	Speed of sound
c_p	Specific heat capacity at constant pressure
c_v	Specific heat capacity at constant volume
F_{fx}	Friction force acting on the control volume projected in the streamwise direction
h	Specific enthalpy
h_f	Heat transfer coefficient
k	Thermal conductivity
M	Mach number
p	Pressure
Q	Heat transferred into the control volume
R	Specific gas constant
s	Specific entropy
T	Temperature
T'	Temperature perturbation
T_w	Temperature at the conjugate interface
U	Streamwise velocity magnitude
u, v, w	Velocity components
W_i	Characteristic variables
Ec	Eckert number
MA	Moving average
Pr	Prandtl number
Re	Reynolds number
Re_τ	Reynolds number based on the friction velocity
St	Stanton number

Subscripts and superscripts

x^*	Reference condition
x^+	Dimensionless distance
x_f	Related to the fluid
x_s	Related to the solid
x_t	Stagnation quantity
x_{SS}	Steady state value

pressure and Mach number that follows the direction of the entropy change. The opposite holds on the supersonic branch. Fig. 1 shows this phenomenon graphically by plotting the contours of the dimensional mass flow change with respect to adiabatic conditions for different inlet Mach number and total temperature increase. At low Mach number ($M_1 < 0.6$), the change in mass flow rate relative to adiabatic condition is less than proportional to the change in total temperature, i.e. a change of 1% in $T_{t,2}$ will lead to a change in mass flow rate less than 1% with respect to the adiabatic case. For $0.6 < M_1 < 1$, the change in mass flow rate becomes more than proportional to $T_{t,2}/T_{t,1}$. As the fluid continues to be heated, the flow eventually becomes thermally choked, resulting in smaller changes in mass flow rate. The unshaded area represents the thermally choked region. On the supersonic side, for most of the Mach number range tested, the change in mass flow rate is more than proportional to the stagnation temperature change. The greatest change in capacity occurs near sonic conditions where $\|\frac{dM}{ds}\|$ is maximum.

Practical examples of how heat transfer can influence flow characteristics can be found in numerous research areas. For instance, in combustor flows [7,8], in transonic compressors [9], and in hypersonic flows [3,10].

1.2. Effects of unsteady conjugate heat transfer through the external walls on flow characteristics

Having reviewed and demonstrated some steady state effects of conjugate heat transfer on a system, we now turn to the impact of unsteadiness. For instance, Fig. 2 sketches the time evolution of a flow quantity for an experiment involving the flow of a hot fluid through equipment of large thermal capacity, initially at room temperature, when CHT is taken into account. The initial transient phase corresponds to the fluid accelerating from rest to a quasi-steady state value from the perspective of fluid time scales. This state, denoted as Γ_{iso}, represents a system with isothermal walls since the large thermal capacity of the metal causes the interface to act as an isothermal boundary. After reaching this point, the variable gradually drifts as the metal approaches thermal steady state, Γ_{SS}. The time required to reach steady state depends on the thermal time scales of the solid.

A practical example can be found in aeroengines, where the time required to reach thermal equilibrium after startup often constitutes a significant portion of the flight envelope, leading to changes in the thermodynamic flow path, as described by Lazareff et al. [11]. Similar transient heat transfer conditions occur during engine start-up and shutdown in rocket propulsion systems. During these transients, the chamber or nozzle walls can reach temperatures higher than those observed during steady state operation and may experience substantial temperature gradients [12]. As a result, cooling systems designed for nominal engine conditions may be inadequate to ensure overall safety and structural integrity. Wang et al. [13] studied the cold start warm-up process of a steam turbine control valve, observing significant changes in temperature and heat flux throughout the startup process.

Hypersonic flows also are highly influenced by heat transfer, and it is widely recognised that outer walls do not reach thermal equilibrium during typical testing due to the rapid nature of the flow. As a result, walls are often modeled as isothermal, based on the assumption that they cannot respond quickly enough within the experiment's duration [14]. However, as reviewed by Lewis and Hickey [3], at high speeds, non-adiabatic wall temperatures significantly affect both the characteristics of the turbulent boundary layer and its transitional behaviour. Griffin et al. [10] proposed a scaling law for the transitional boundary layer thickness in hypersonic flows, emphasising the importance of accounting for non-adiabatic wall temperatures in such cases. Recently, [15] studied the mechanisms governing the unsteady interactions between a showckwave and a boundary layer.

Another area where thermal transients are of significant interest is experimental testing. Often, the temperature field of the test section is not matched to the target conditions. For example, turbine testing typically involves cooler test chamber walls compared to actual turbine walls. This mismatch can result in spurious temperature gradients and heat transfer from external surfaces, potentially compromising measurement accuracy. A practical example of this was observed by Adams et al. [16] during the design of a swirler for a transonic test turbine facility. They reported a 6% reduction in the mass-mean total temperature at the turbine inlet, which was attributed to convective heat transfer to the metal components.

From a transient perspective, many test facilities operate for a short duration, typically on the order of a few seconds. This limited

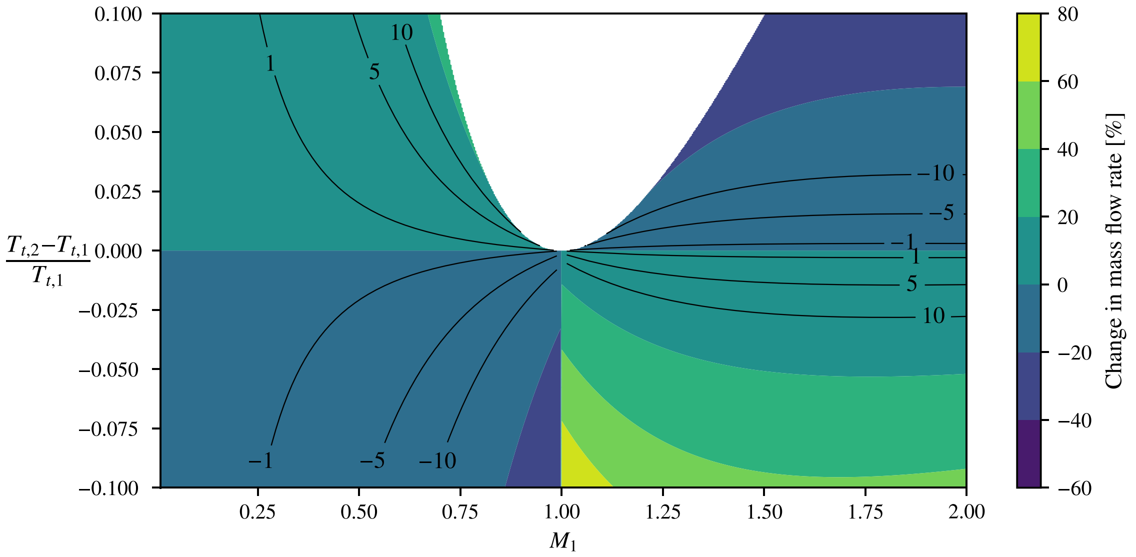

Fig. 1. Contours of the relative change in dimensional mass flow rate with respect to adiabatic conditions at fixed stagnation temperature and Mach number.

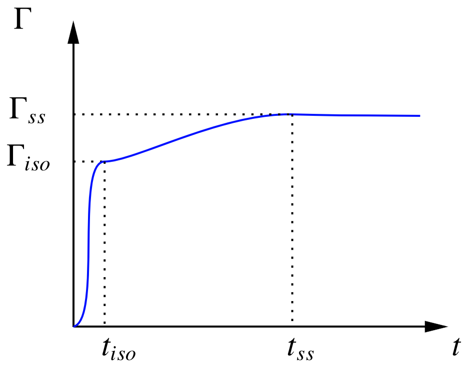

Fig. 2. Sketch of the typical unsteady behaviour of a global flow quantity with external heat transfer.

timeframe frequently proves often insufficient for solid components to achieve thermal equilibrium with the fluid. Measurements taken during this period would correspond to t_{iso}, as shown in Fig. 2. These slow thermal transients can significantly impact flow dynamics in high-temperature applications, particularly when tests are conducted in quick succession. Amend et al. [17] addressed this issue in their study of a lean-burn combustor simulator by implementing a transient effectiveness correction to account for convective heat loss to the endwalls.

Similarly, when calibrating total temperature probes, Englerth [18] found that repeatability and sensor performance were highly dependent on the thermal state of the stainless steel facility. To ensure accurate measurements, they ran the facility until the nozzle reached a steady state temperature, minimising heat transfer between the fluid and the structure, which otherwise affected total temperature readings and sensor accuracy. Achieving steady state conditions greatly improved measurement repeatability.

In transient heat transfer studies, thermal transients have been shown to affect external wall heat transfer characteristics. Bianchi et al. [19] studied unsteady heat conduction in nozzles and its impact on erosion. Their results indicated that the steady state condition was achieved near the throat region, while regions farther from the throat — experiencing lower heating rates — remained far from steady state. Xue et al. [20] developed a transient measurement technique for heat transfer that accounts for linear temperature variations in the main flow during the measurement window due to cooling.

These examples underscore the importance of unsteady heat transfer effects in practical situations, as they can significantly alter both local and global flow parameters. Researchers must be aware that their experiments capture either Γ_{iso} or Γ_{SS}; otherwise, time-dependent modeling errors may be introduced. These steady and unsteady phenomena are often overlooked in standard testing procedures, where measurements rarely account for the influence of external heat transfer.

A similar argument can be made from a computational perspective. Most numerical methods do not account for CHT; the interface between solid walls and fluid domains is typically modeled using simplified thermal boundary conditions, such as fixed heat flux or constant temperature. The isothermal boundary condition represents rapid transients, where swift changes in state parameters preclude significant heat transfer. This assumption implies that the surrounding environment has infinite heat capacity, corresponding to the Γ_{iso} state from Fig. 2. Conversely, constant heat flux boundaries, particularly the limiting case of adiabatic flow, assume that the gas has achieved thermal equilibrium with its surroundings. This condition is usually associated with slow, time-dependent processes. Except for high-temperature cases, the adiabatic or isothermal boundary assumptions are widely adopted as default boundary condition in numerical simulations for blade and end walls. Only for thermal assessments of turbine blades or combustors is heat transfer to the solid taken into account, and even then, it is often done in a steady state manner. This simplification represents a significant limitation that must be carefully considered during the validation or calibration of CFD results against experimental data.

The reason time-accurate conjugate heat transfer is rarely accounted for in numerical simulations is because it faces significant challenges. These arise primarily due to the substantial disparity between thermal time scales of solids and fluids. Conventional numerical methods, such as URANS or LES, rely on time-marching approaches with small timesteps. When combined with stringent grid requirements for the solid domain, these methods become computationally intensive for conjugate simulations spanning solid thermal time scales.

Reduced-order models offer a promising alternative for capturing both steady and transient CHT effects. These models can provide rapid insights, enabling efficient analysis of CHT impacts and facilitating the development of mitigation strategies. This study will then also aim to assess the ability of simplified models to get order of magnitude estimates and to explore potential mitigation strategies of the slow transients effect.

To further understand the parameters that govern the approach to steady state of the coupled fluid-solid system, we propose a simple

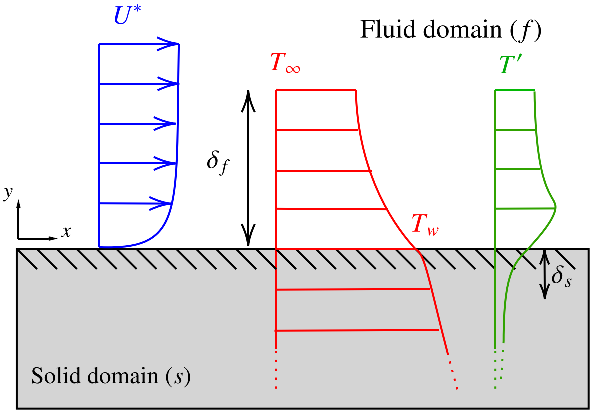

Fig. 3. Sketch of the fluid boundary layer and solid domain.

dimensional analysis of a boundary layer flow. The problem of interest consist of a semi-infinite solid domain in contact with a fluid. The fluid has a streamwise freestream velocity U^* and freestream temperature T_∞. The fluid has some arbitrary temperature fluctuation profile T' associated with a thermal penetration depth δ_s in the solid. A sketch of the problem is available in Fig. 3.

The energy equation for an incompressible boundary layer in coordinates aligned with the surface is given by:

$$\rho_f c_{p,f}\left(\frac{\partial T}{\partial t}+u\frac{\partial T}{\partial x}+v\frac{\partial T}{\partial y}\right)=k_f\frac{\partial^2 T}{\partial y^2}+\mu\left(\frac{\partial u}{\partial y}\right)^2 \tag{3}$$

where u and v are velocity components in x and y directions respectively, t is time, T is temperature, k_f is the thermal conductivity of the fluid, μ is the dynamic viscosity, ρ_f is the density of the fluid and $c_{p,f}$ is the specific heat capacity at constant pressure. The dissipation term is included to ensure the analysis is applicable to both subsonic and transonic flows.

On the solid side, the unsteady heat equation applies. Assuming that the streamwise characteristic length scale is much larger than the transversal one, the streamwise heat diffusion can be neglected. The energy equation for the solid is then given by:

$$\rho_s c_{p,s}\left(\frac{\partial T}{\partial t}\right)=k_s\frac{\partial^2 T}{\partial y^2} \tag{4}$$

where k_s is the thermal conductivity of the solid, ρ_s is the density of the solid and $c_{p,s}$ is the specific heat capacity.

At the interface, we have the continuity of both the heat flux and the temperature:

$$k_s\left.\frac{\partial T}{\partial y}\right|_s=k_f\left.\frac{\partial T}{\partial y}\right|_f \quad \& \quad T|_s=T|_f \tag{5}$$

On the fluid side, introducing the following dimensionless variables:

$$\tilde{u}=\frac{u}{U^*},\ \tilde{v}=\frac{v}{U^*},\ \tilde{t}=t\frac{U^*}{L^*},\ \tilde{x}=\frac{x}{L^*},\ \tilde{y}=\frac{y}{\delta_f},\ \tilde{T}=\frac{T-T_\infty}{T_w-T_\infty}$$

Where L^* is a characteristic length scale in the streamwise direction, U^* is the characteristic streamwise velocity, T_w is the interface temperature and δ_f is the thermal boundary layer thickness of the fluid domain.

$$\frac{\partial\tilde{T}}{\partial\tilde{t}}+\tilde{u}\frac{\partial\tilde{T}}{\partial x^*}+\tilde{v}\frac{\partial\tilde{T}}{\partial y^*}=\frac{1}{\mathrm{Re}\ \mathrm{Pr}}\left(\frac{L^*}{\delta_f}\right)^2\frac{\partial^2\tilde{T}}{\partial\tilde{y}^2}+\frac{\mu L^*}{\rho_f c_{p,f}U^*(T_w-T_\infty)}\left(\frac{U^*}{\delta_f}\right)^2\left(\frac{\partial\tilde{u}}{\partial\tilde{y}}\right)^2 \tag{6}$$

Introducing the Eckert number Ec:

$$\frac{\partial\tilde{T}}{\partial\tilde{t}}+\tilde{u}\frac{\partial\tilde{T}}{\partial x^*}+\tilde{v}\frac{\partial\tilde{T}}{\partial y^*}=\frac{1}{\mathrm{Re}\ \mathrm{Pr}}\left(\frac{L^*}{\delta_f}\right)^2\frac{\partial^2\tilde{T}}{\partial\tilde{y}^2}+\frac{\mathrm{Ec}}{\mathrm{Re}}\left(\frac{L^*}{\delta_f}\right)^2\left(\frac{\partial\tilde{u}}{\partial\tilde{y}}\right)^2 \tag{7}$$

Eq. (7) can be further simplified using the desired scaling for the Reynolds number and the streamwise to transversal characteristic length scale ratio $\left(\frac{L^*}{\delta_f}\right)\sim\mathrm{Re}^{\ a}$.

$$\text{General BL:}\quad \frac{\partial\tilde{T}}{\partial\tilde{t}}+\tilde{u}\frac{\partial\tilde{T}}{\partial x^*}+\tilde{v}\frac{\partial\tilde{T}}{\partial y^*}=\frac{\mathrm{Re}^{-1+2a}}{\mathrm{Pr}}\frac{\partial^2\tilde{T}}{\partial\tilde{y}^2}+\mathrm{Ec}\mathrm{Re}^{-1+2a}\left(\frac{\partial\tilde{u}}{\partial\tilde{y}}\right)^2 \tag{8}$$

For instance, in a laminar boundary layer the proportionality relation is given by $\left(\frac{L}{\delta_f}\right)\sim\sqrt{\mathrm{Re}}$ which would lead to Eq. (9).

$$\text{Laminar BL:}\quad \frac{\partial\tilde{T}}{\partial\tilde{t}}+\tilde{u}\frac{\partial\tilde{T}}{\partial x^*}+\tilde{v}\frac{\partial\tilde{T}}{\partial y^*}=\frac{1}{\mathrm{Pr}}\frac{\partial^2\tilde{T}}{\partial\tilde{y}^2}+\mathrm{Ec}\left(\frac{\partial\tilde{u}}{\partial\tilde{y}}\right)^2 \tag{9}$$

In Eq. (8), the approach to a steady state is dominated by the diffusion coefficient, $\left(\frac{\mathrm{Re}^{-1+2a}}{\mathrm{Pr}}\right)$, in front of the second order term. The nonlinear term and the convective terms can also affect the approach to equilibrium especially at the initial state when the flow has not settled yet to a quasi-steady state, but the second-order derivative term is generally the dominant factor in determining the approach to steady state rate.

For the solid domain, we introduce the dimensionless transversal coordinate on the solid side $\tilde{y}_s=\frac{y}{\delta_s}$, based on the thermal boundary layer thickness. The interface condition can be rewritten as:

$$\frac{k_s}{\delta_s}\left.\frac{\partial\tilde{T}}{\partial\tilde{y}_s}\right|_s=\frac{k_f}{\delta_f}\left.\frac{\partial\tilde{T}}{\partial\tilde{y}}\right|_f \tag{10}$$

Assuming the gradients of the normalised temperature with respect to the dimensionless transversal coordinate specific to the individual domains are of the same order, we have:

$$\frac{\delta_s}{\delta_f}\sim\left(\frac{k_s}{k_f}\right) \tag{11}$$

Finally, the unsteady heat equation in the solid can be made dimensionless:

$$\frac{\partial\tilde{T}}{\partial\tilde{t}}=\frac{L^*}{U^*}\frac{\alpha_s}{\delta_s^2}\frac{\partial^2\tilde{T}}{\partial\tilde{y}_s^2} \tag{12}$$

Under the assumption that in the boundary layer $h_f=k_f/\delta_f$, we have:

$$\frac{\partial\tilde{T}}{\partial\tilde{t}}=\frac{L^*}{U^*}\frac{\alpha_f}{\alpha_f}\frac{\alpha_s}{\delta_s^2}\frac{\partial^2\tilde{T}}{\partial\tilde{y}_s{}^2}=\frac{\partial\tilde{T}}{\partial\tilde{t}}=\frac{L^*\delta_f}{\delta_s^2}\frac{\alpha_s}{\alpha_f}\mathrm{St}\frac{\partial^2\tilde{T}}{\partial\tilde{y}_s{}^2} \tag{13}$$

Using the proportionality found in the interface equation, we have the final equation for the solid side:

$$\frac{\partial\tilde{T}}{\partial\tilde{t}}=\frac{L^*}{\delta_s}\frac{\rho_f c_{p,f}}{\rho_s c_{p,s}}\mathrm{St}\frac{\partial^2\tilde{T}}{\partial\tilde{y}_s{}^2}=\frac{\delta_f}{\delta_s}\frac{\rho_f c_{p,f}}{\rho_s c_{p,s}}\frac{\mathrm{Re}^a}{\mathrm{St}}\frac{\partial^2\tilde{T}}{\partial\tilde{y}_s{}^2} \tag{14}$$

$$=\frac{k_f\rho_f c_{p,f}}{k_s\rho_s c_{p,s}}\frac{\mathrm{Re}^a}{\mathrm{St}}\frac{\partial^2\tilde{T}}{\partial\tilde{y}_s{}^2} \tag{15}$$

In Eqs. (8) and (15), the diffusion coefficients determine how quickly the system approaches steady state. On the fluid side from Eq. (8), shows that the diffusion coefficient is dependent on the Prandtl number and the Reynolds number scaling of the boundary layer height. On the solid side, Eq. (15), the approach to steady state depends on the thermal capacity ratio of the solid to the fluid, the ratios of heat conductivities, the Stanton number and again on the Reynolds number. In Eq. (15), the product $k\rho c_p$ appear which is characteristic of transient thermal analysis because it directly influences the rate at which heat is absorbed, stored, and conducted within a material, [21].

For a typical, fluid-solid coupled system of air and steel the following properties can be chosen. The metal specific heat is 465 J/kg K, thermal conductivity 54 W/(m K) and density 7800 $\mathrm{kg/m^3}$. The

Prandtl number of air is of order 1, thermal conductivity 3×10^{-2}W/(m K), density 1.293 kg/m^3 and specific heat capacity 1000 J/kg K. The Stanton number of the coupled system is $\approx\ 10^{-1}$ with a Reynolds number of 100,000.

Using these values, in a turbulent boundary layer, the ratio between the diffusion constants of the two equations become:

$$\frac{\frac{k_f \rho_f c_{p,f}}{k_s \rho_s c_{p,s}} \mathrm{StRe}^a}{\left(\frac{\mathrm{Re}^{-1+2a}}{\mathrm{Pr}}\right)} \simeq 4\cdot 10^{-4} \tag{16}$$

Eq. (16) shows that the ratio of the diffusion constants is of the order of 10^{-4}. Indicating that, if the system was decoupled, the fluid side would reach a steady state much faster than the solid side. However, in the coupled system, the solid side will influence the fluid side, and the system will reach a steady state at a rate determined by the solid side, forcing the simulation or experiment to be carried out for extended time periods. Besides the physical properties of the system, the main parameters that describe this ratio are the Stanton number, which directly describes the interface condition, and the Reynolds number. A similar result for the time scales' ratio was obtained by He and Oldfield [22], who noted that in typical operating conditions, the ratio of these time scales is approximately 10,000.

The aim of the paper is to illustrate the impact of unsteady CHT on global flow quantities. To this end, we will simulate numerically the transient flow through a nozzle with conducting walls. The global flow quantity of interest chosen is capacity, which will be recorded over time, similarly to Fig. 2, to see how it evolves. The transient evolution will be characterised by the parameters governing the approach to steady state of the coupled fluid-solid system.

1.3. Capacity prediction

Flow capacity can be defined as:

$$\Gamma = \frac{\dot{m}\sqrt{T_t}}{p_t} \tag{17}$$

In axial turbomachinery, accurate capacity measurements has been a long-standing challenge and area of research interest [23,24]. The capacity of the high-pressure nozzle guide vane (NGV) typically plays a critical role in design as it sets the overall engine capacity. Inaccurate prediction of engine capacity leads to mismatching of downstream stages, where even minor deviations from design conditions can significantly impact performance. .wf/10.5772/intechopen.74104 Despite technological advancements, there remains a noticeable discrepancy between engine test capacity measurements and those obtained through alternative methods. Previous research has identified various potential sources for this discrepancy. From a numerical perspective, Fielding [25] provided insights on the relationship between irreversibilities and capacity measurements in gas turbines and introduced a correction factor to account for this effect. Afanasiev et al. [26] put forward the influence of 3D flow effects on capacity measurements by comparing 1D and 3D approaches. Experimentally, Povey [24] studied the effect of film cooling on capacity measurements. Burdett et al. [27] presented a novel technique for low uncertainty capacity measurements. CHT can significantly affect capacity measurements and predictions due to the extreme operating conditions of NGVs. These components typically function in high-pressure, high-temperature environments, often approaching 1500 °C.

2. Methodology

The present numerical study will use two methods to investigate the impact of unsteady conjugate heat transfer and these methods are outlines in this section. First, an unsteady quasi-one-dimensional analysis utilising the method of characteristics (MOC). This is used to get an estimate on the time scales and bounds of the CHT influence. It is anticipated that this reduced order method will adequately capture slow thermal transients, while the influence of turbulent perturbations on the system will not be captured. Then, fully coupled Large Eddy Simulations (LES) will serve as baseline cases.

2.1. Unsteady, quasi-one-dimensional compressible flow with heat transfer (MOC)

The method of characteristics provides a straightforward approach to solving the unsteady Euler equations [28–30]. It has also been successfully applied to simulate efficiently unsteady flows with heat transfer. Issa and Spalding [31] presented a procedure for solving one-dimensional, unsteady, compressible, frictional flows with heat transfer, demonstrating its effectiveness in simulating shock tube flows. Similarly, Huang [32] employed the method of characteristics to study unsteady flow in a heat exchanger. The unsteady Euler equations can be transformed into the characteristic expression written in Eq. (18), details of the derivation are available in Appendix B. The source vector of the conservative variables has been projected and behave as source terms for the entropy and the sounds waves.

$$\begin{aligned}
\frac{\partial W_1}{\partial t} &= -U & &\frac{\partial W_1}{\partial x} & &-(\gamma-1)\frac{\rho U}{a^2}\delta Q_x \\
\frac{\partial W_2}{\partial t} &= -(U+a) & &\frac{\partial W_2}{\partial x} - Ua\frac{1}{A}\frac{dA}{dx} & &+(\gamma-1)\frac{U}{a}\ \delta Q_x \\
\frac{\partial W_3}{\partial t} &= -(U-a) & &\frac{\partial W_3}{\partial x} + Ua\frac{1}{A}\frac{dA}{dx} & &-(\gamma-1)\frac{U}{a}\ \delta Q_x
\end{aligned} \tag{18}$$

The conjugate portion of the code solves the unsteady heat conduction equation in a 2D finite element framework fully coupled with the MOC. Unlike the MOC, wall-normal temperature variations are considered with both streamwise and wall-normal conduction solved for. The interface condition is imposed by continuity of the heat flux. The heat flux can be inferred from the temperature difference between the fluid and the solid and a correlation for the heat transfer coefficient, for instance the Dittus–Boelter equation for turbulent flows in tubes.

2.2. 3D Large Eddy Simulations (LES)

The flow equations are solved using the in-house code H4X [33–36]. The code is a cell-centred finite volume code based on a multiblock grid arrangement. The flow field is represented by the viscous variables: velocities, temperature, pressure. The equations of motion for a compressible fluid are solved in conservative form. The spatial discretisation is third-order accurate in space for the inviscid fluxes. Third-order accuracy is achieved on a compact stencil by using variable extrapolation. No limiter is applied to the entropy and vorticity fields whereas the sound waves are limited using a third order limiter introduced by [37]. The extrapolation is based on weighted least-square gradients. The gradient stencil contains all the face neighbours of each cell. For the purpose of variable extrapolation onto a cell interface, the gradient stencil is biased by removing the contributions from the neighbour on the other side of the interface. At low Mach numbers, the numerical fluxes are adapted following the work of Hope-Collins and di Mare [34] and a modified pressure flux is employed. The viscous fluxes are evaluated using a second-order discretisation. Advancement in time is performed using a formally second-order accurate implicit scheme. The implicit iterations are based on a dual-time stepping formulation. The dual-time framework is advantageous for unsteady problems with multiple time scales, such as CHT problems. It allows for the separation of these scales, enabling each to be resolved appropriately without the need for excessively small physical time steps. The code is parallelised by partitioning the blocks of the multiblock grid among the available MPI ranks. Within each rank, block operations are parallelised using OpenMP. Computations and communications are overlaid to hide the latency of the network fabric. The computations have been done on the Cirrus UK National Tier-2 HPC Service.

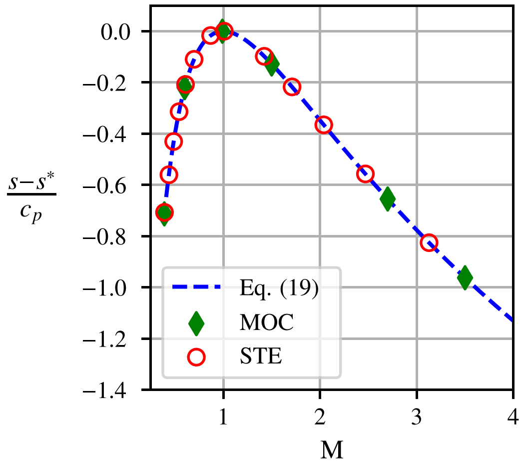

Fig. 4. Validation of the steady state Rayleigh flow for the STE and MOC methods.

At the inflow boundary, synthetic turbulence is generated using the method described by Dreze et al. [33]. This technique uses modified uniformly distributed random sequences to construct divergence-free anisotropic random fields with sensible spectrum and complete complex correlation in space and time.

The conjugate portion of the code solves the unsteady heat conduction equation in a fully-coupled fashion using a node-based finite element framework. The solid domain mesh is directly extruded from the interface surface and the mesh is scaled proportionally to the wall-normal mesh density of the fluid domain. This technique avoids the requirements of generating two separate meshes and as well as the overheads related to a separate data structures for the solid grid and provisions for interpolation of temperatures and fluxes between the two grids. The extrusion uses a thin layer approximation to form the heat conduction equation. The Laplacian of the temperature in a thin layer for geodesic coordinates on a smooth surface can be written as:

$$\mathcal{L}(T) = \frac{\partial^2 T}{\partial \xi^2} + \frac{\partial^2 T}{\partial \eta^2} + \frac{\partial^2 T}{\partial \zeta^2} + \frac{1}{R_c}\frac{\partial T}{\partial \zeta} \tag{19}$$

where $\frac{1}{R_c}$ is the local harmonic mean curvature of the surface.

3. Results

This section studies two different cases. First, a Rayleigh flow is used to validate the different conjugate methods. Then, as Fig. 1 showed that the effect of heat transfer on a discharge characteristic of quasi-one-dimensional flow is strongest near sonic conditions, a transonic nozzle is simulated and the transient evolution of capacity is recorded.

3.1. Channel with uniform heat flux

To validate the inviscid MOC and the steady approach proposed, a Rayleigh flow is used. The dimensionless change in entropy with respect to sonic conditions has been derived in Shapiro [38] and is shown in Eq. (20). Fig. 4 compares this theoretical solution with the different implementations to demonstrates agreement of the solutions for this reference case for the inviscid approaches. In all cases the entropy change has been applied as a constant uniform heat flux along the length of the domain.

$$\frac{s-s^*}{c_P} = \ln\left[M^2\left(\frac{\gamma+1}{1+\gamma M^2}\right)^{(\gamma+1)/\gamma}\right] \tag{20}$$

To validate the LES methodology, the present methodology is compared to simulations by Kawamura et al. [39]. They simulated heated channel flows with symmetrical heating from both walls. The heating is applied using a uniform constant heat flux. To keep the energy balanced, a negative source term is applied to the energy equation. The bulk Reynolds number is 5500 corresponding to a Reynolds number based on the friction velocity of 180 and the inlet Mach number is 0.1, to align best with the incompressible results from Kawamura et al. [39]. The Prandtl number is set to 0.71. The streamwise length of the computational domain is $8\pi\delta$ while the transversal length is $4/3\pi\delta$ where δ is the channel half-width. The first section of length $3\pi\delta$ section was used for the inflow generated fluctuations to settle, and the heat flux was only applied to the remaining of the domain. The grid has a stretching in the wall-normal directions detailed in [40] and grid statistics can be found in Table 1. The mean normalised temperature θ^+ profile is shown in Fig. 5 and shows good agreement with Kawamura et al. [39]. Towards the middle of the channel, the temperature profile is overpredicted by a maximum of 3.7%.

Table 1
Grid statistics for the channel flow simulation.

M_1	Re_τ	(N_x, N_y, N_z)	Δx^+	Δy^+	Δz^+
0.1	178.38	(312, 144, 128)	14.34	0.31	5.92

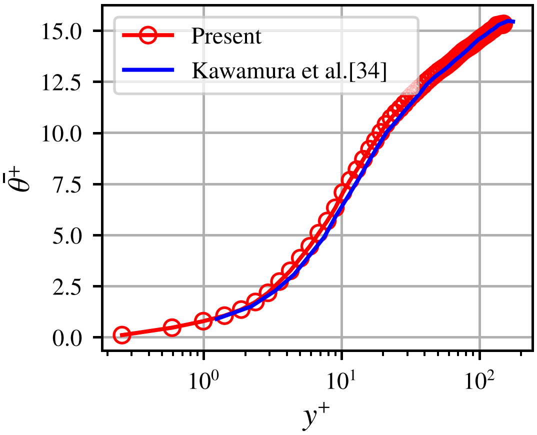

Fig. 5. Mean dimensionless temperature profile for the channel flow.

Now that both approaches have been validated, let us investigate the transient evolution of flow capacity. The channel was started from rest and the capacity was recorded. The transient evolution of the normalised capacity is shown in Fig. 6 , the time is normalised by the channel flow through time, defined as the length of the channel divided by the bulk velocity. In this case the time to reach steady state is relatively short in terms of fluid time scales because the boundary condition is time invariant. The capacity predictions by the quasi one-dimensional methods are accurate within a couple of percents and can be attributed to boundary layer blockage, effectively reducing the core flow area. This is a well-known phenomenon limitation and multiple correction methodologies to account for viscous effects and boundary layer growth have been proposed in the literature, [41,42].

3.2. Back nozzle

The transonic case examined is an axisymmetric convergent-divergent nozzle, originally studied by Back et al. [43]. The primary objective of their study was to collect experimental data on convective heat transfer in turbulent flows characterised by significant pressure gradients, where boundary layers where relatively thin compared to the channel cross-section.

The specific configuration involves a nozzle discharging a perfectly expanded isothermal free jet at Mach 2.4 for a Reynolds number based on the throat radius of Re= 4.1×10^4 and a Reynolds number based on the friction velocity $\mathrm{Re}_\tau = 993$, with a pressure ratio of 11.

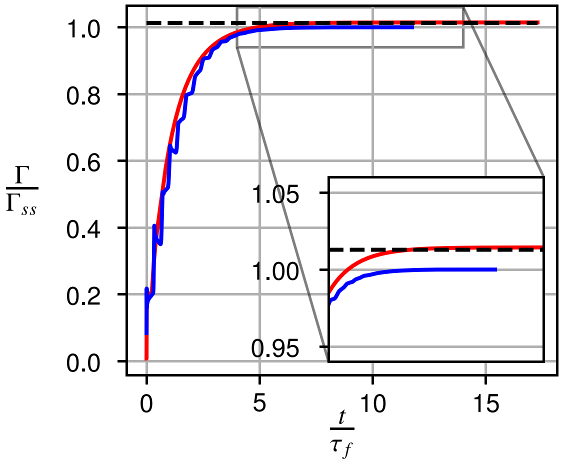

Fig. 6. Transient evolution of capacity normalised by the steady state capacity value of the LES. Black curve is steady method, red curve is MOC and blue curve is LES results. (For interpretation of the references to colour in this figure legend, the reader is referred to the web version of this article.)

The boundary conditions at the nozzle inlet are set to a stagnation temperature of 833 K and a pressure of 10.34 bar. The freestream boundary condition is established at standard atmospheric pressure and room temperature. This case serves as an excellent test scenario due to the extensive available data on heat transfer. The nozzle external walls are made of 8 mm thick 502-type stainless steel and are assumed to be thermally insulated to the exterior.

The grid used for this case is a structured radial grid with a conformal elliptic transformation to an axisymmetric domain with a power law stretching at the walls. The grid size is (288 × 128 × 128). This leads to a grid spacing of Δy^+ in the range $[0.71, 3.27]$ on the fluid side and $[0.32, 1.46]$ on the solid side. The mesh on the solid side is finer at the wall because the lower penetration depth in the solid requires appropriate resolution to capture correctly the wall fluctuations, as per Eq. (11). The streamwise spacing was adjusted so that it lied in the range $\Delta x^+ \in [10, 45]$. The domain extends 3 nozzle diameters upstream of the nozzle inlet to allow for the synthetic turbulence to morph into the prescribed turbulent profiles. The profiles are fully turbulent following a 1/7-power-law curve as reported in [43]. Once thermal steady state reached for the combined system, the simulations were run for 10 flow-through times to record steady state statistics. CHT is not considered in the extended upstream domain.

Fig. 7 shows the convective heat-transfer coefficient of the LES results, and comparison to data extracted from Back et al. [43]. The largest difference between the experimental data and the LES results is downstream of the nozzle throat towards the exit of the nozzle where the relative difference is 19%. LES data is also compared with a finer grid of 288 × 160 × 160 with adiabatic walls, to show consistency and appropriate resolution. Even if the finer grid captures better the heat transfer coefficient peak at the throat the maximum difference between the two grids is less than 5% for the heat transfer coefficient. The difficulty in predicting the divergent section has been noted in previous studies [44–46] and despite some discrepancies, the main trend is well captured, reinforcing confidence in the overall results. Table 2 compares also macroscale properties of the different cases, confirming the ability of the chosen grid to simulate the desired setup.

For the MOC approach the heat transfer coefficients were directly taken from the experimental data.

The transient behaviour of the nozzle is shown in Figs. 8 and 9, the dark blue line correspond to a moving average (MA) value while the light blue is the instantaneous value. Fig. 8 shows the initial startup period that ends when the first pseudo steady state is reached. Fig. 9 then plots the slow capacity drift that occurs because of the external walls are heating up before reaching a final steady state. In both plots the dimensionless time has been normalised by the constants found in Section 1.2.

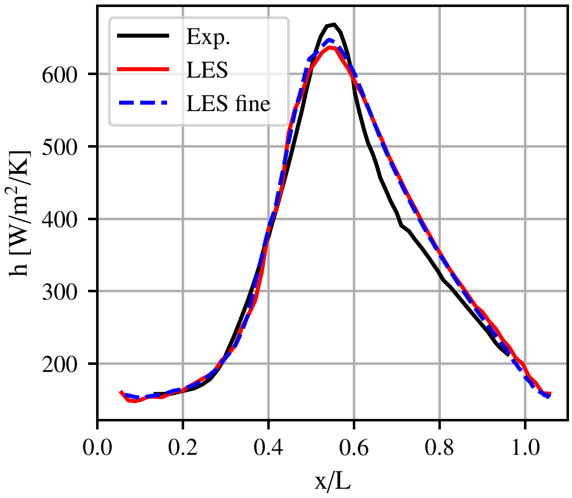

Fig. 7. Steady heat transfer coefficient for the Back nozzle.

Table 2
Global properties of the cases for the Back nozzle.

	Back et al.	LES	Finer LES (adiabatic)
M_2	2.45	2.42	2.41
St $\times 10^3$	1.58	1.50	1.53
$\Gamma \times 10^5$ $[m\sqrt{K}s]$	6.46	6.31	6.34

For both the LES and the MOC, the capacity in the initial pseudo steady state is higher than the final steady state value. For instance, as seen in Fig. 9, the pseudo steady state value for the LES case is $\Gamma = 6.42 \times 10^{-5}$ while the final steady state value is $\Gamma = 6.11 \times 10^{-5}$. The overprediction comes from the fluid being overcooled because of the initial temperature difference between the walls and the flow. This leads to denser flow and therefore greater mass flux. Therefore, as per Fig. 9, if the external walls are not at thermal steady state, the capacity will be overpredicted by 1.7%. Looking at the comparison between the LES and MOC predictions for the final value of capacity, the quasi one dimensional method fall within 2% of the LES predictions. Similarly to Section 3.1, while the one-dimensional model fails to capture the boundary layer blockage effect, the differences in the predictions remain low due to the relatively simple geometry and thin boundary layers. But the transient behaviour of capacity is well captured by the MOC method. In terms of computational efficiency, the 1D MOC method completes within a minute on a standard laptop, whereas the full transient conjugate LES simulation requires access to large multicore facilities. This stark contrast underscores the practicality of MOC for rapid analysis.

The transient behaviour of capacity has the characteristic exponential decay of a preheated body cooled by convection. The characteristic time of the decay to steady state depends on the solid thermal properties and the heat transfer coefficient. When superimposed, one can see that the capacity decay in the LES case is lagging in time with respect to the one-dimensional model and has narrower bounds. This is because the boundary layer acts as a thermal resistance for heat transfer, slowing down the rate of heat transfer between the surface and the fluid. The fluid in direct contact with the cold surface quickly cools down and loses heat, while the faster-moving fluid above this layer does not lose heat as quickly. Resulting in additional time for the heat flux that is lost to the external wall to reach the mean flow, the amplitude is also lower because not all the heat transferred is reaching the mean

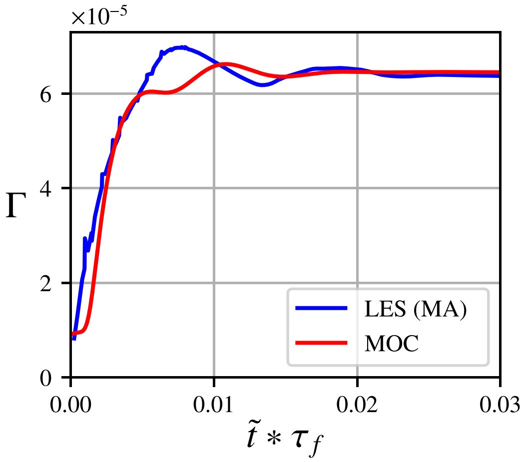

Fig. 8. Time evolution of the nozzle capacity starting from rest. (For interpretation of the references to colour in this figure legend, the reader is referred to the web version of this article.)

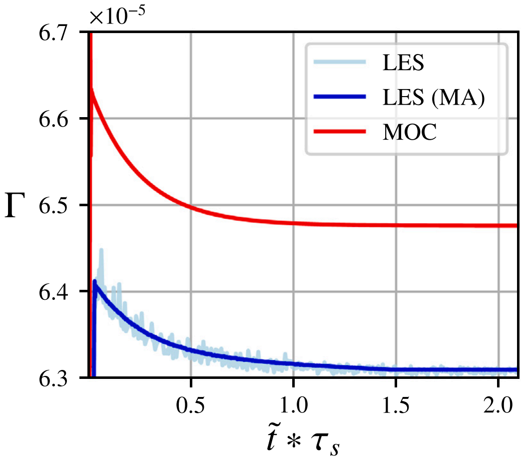

Fig. 9. Time evolution of the nozzle capacity after the initial startup transient. (For interpretation of the references to colour in this figure legend, the reader is referred to the web version of this article.)

flow. The thicker the boundary layer, the greater the resistance to heat transfer.

This phenomenon has been well-known and quantified for critical flow Venturi (CFV) nozzle, warmer, lower density gas near the CFV wall reduces mass flux through the CFV, an effect that increases in significance at lower Reynolds numbers. Wright et al. [47] proposed a correction factor for the thermal boundary layer effect. Wang et al. [48],Ding et al. [49] also studied this effect experimentally and numerically and concluded that it can have great impact on the mass flow.

To reduce the time required for the thermal transient to vanish, one solution is to preheat the walls to try to lower the initial temperature difference. Fig. 10 plots a case where the external walls have been preheated to 75% of their steady state temperature rise.

During the thermal transient, the temperature difference in the metal decays exponentially, and the temperature distribution in the solid stays self-similar, if streamwise conduction can be ignored. This is because while the time constant of the solid is only related to the thermal properties of the system, the bounds of the decay are directly proportional to the fluid-solid temperature difference at the first pseudo-steady state.

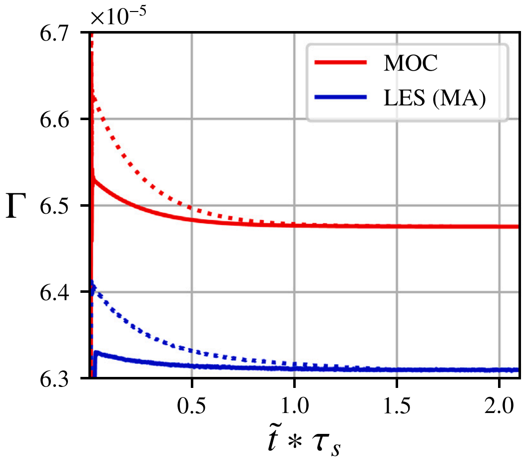

Fig. 10. Effect of preheating on the capacity evolution. Dotted lines are non-preheated cases, while solid lines are preheated cases.

4. Conclusion

This article has presented a comprehensive study of the existing research on the influence of external heat transfer on flow characteristics. Until thermal steady state is reached, all flow quantities are drifting, and this transient can be significant in case of high-temperature gradients between the initial solid thermal state and the steady state value. The study has focused on a practical application using capacity prediction to demonstrate these effects and to assess on the ability of simple models to predict the range of impact. For the transonic nozzle case, the error made if the external heat loss is not taken into account is about 2%. However, in other scenarios and quantity of interest it can have a greater impact, as reported by [16].

It was concluded that these methods are well suited to predict the global effects of heat loss. The literature survey showed that only few research items talk about this issue, but researcher could benefit with the use of 1D models to better design for this phenomenon. While for more complex cases, the predicted values might be offset because of unaccounted for 3D effects or other, the authors believe that the extent of the influence of CHT will still be well captured due to its intrinsic influence on the coreflow.

Finally, one strategy to minimise the effects of the slow thermal transients is to pre-heat the external walls to reduce the time to reach a steady state. While the exponential decay of the capacity will be self-similar, the amplitude of the decay will be directly proportional to the initial temperature difference.

A notable limitation of this study is the scarcity of experimental data for validation, as existing high-temperature experiments rarely comment on the thermal equilibrium or report time-resolved temperature fields. Future transient thermal tests cases would be valuable for cross-validating the numerical results.

CRediT authorship contribution statement

Yann Dreze: Writing – review & editing, Writing – original draft, Validation, Software, Methodology, Investigation. **Luca di Mare:** Writing – review & editing, Supervision.

Declaration of competing interest

The authors declare that they have no known competing financial interests or personal relationships that could have appeared to influence the work reported in this paper.

Acknowledgements

The authors are grateful for the support from Rolls-Royce PLC and the EPSRC Center for Doctoral Training in Future Propulsion and Power. The authors would also like to acknowledge the use of the Cirrus UK National Tier-2 HPC Service at EPCC (http://www.cirrus.ac.uk) funded by the University of Edinburgh, United Kingdom and EPSRC, United Kingdom (EP/P020267/1). The authors would like also to thank Andrew Oliva for their helpful advice.

Appendix A. Equations for steady, quasi-one-dimensional compressible flow with heat transfer (ste)

The equations for steady non-isentropic internal flows have long been a subject of theoretical interest. Classical cases such as Fanno and Rayleigh flows have analytical solutions [38,50] and multiple set of solutions for other types of flow have been proposed [51–53]. This paper adopts the methodology proposed by Oliva and Morris [54], who presented a closed-form solution for internal compressible flows with an arbitrary combination of area change, heat addition, friction, and non-uniform flow. Both friction forces and heat transfer are expected to influence the mass flow.

Consider a control volume with varying area, friction, and heat addition as illustrated in Fig. A.11, the following equations can be derived. Using averaged quantities, the mass and momentum conservation equations for this control volume can be derived as follows:

Mass conservation :

$$A_1\rho_1U_1 = A_2\rho_2U_2 \tag{A.1}$$

$$\Leftrightarrow \frac{p_2A_2}{p_1A_1}\sqrt{\frac{T_{t,1}f(M_2)}{T_{t,2}f(M_1)}}\frac{M_2}{M_1} - 1 = 0 \tag{A.2}$$

$$\text{With } f(M) = 1 + \frac{\gamma-1}{2}M^2 \tag{A.3}$$

x-momentum conservation :

$$\rho_2U_2^2A_2 - \rho_1U_1^2A_1 = p_1A_1 - p_2A_2 + \int_{A_1}^{A_2} p\,dA - F_{fx} \tag{A.4}$$

The flow variables in the above equations are representative variables defined by the chosen averaging method. For a detailed discussion on this, refer to [54]. In Eq. (A.4), the streamwise integral for the resultant pressure force acting on the control volume can be simplified by assuming a linear pressure variation with area, as discussed by [54,55]. This allows to rewrite Eq. (A.4) as:

$$p_1A_1(1+\frac{A_2}{A_1}+2\gamma M_1^2) = p_2A_2(1+\frac{A_1}{A_2}+2\gamma M_2^2) - 2F_{fx} \tag{A.5}$$

By combining the continuity and streamwise momentum equations, and neglecting friction forces, we obtain:

$$\frac{(1+\frac{A_2}{A_1}+2\gamma M_2^2)}{(1+\frac{A_1}{A_2}+2\gamma M_1^2)}\sqrt{\frac{T_{t,2}f(M_1)}{T_{t,1}f(M_2)}}\frac{M_1}{M_2} - 1 = 0 \tag{A.6}$$

Eq. (A.6) is a second-order equation for the exit Mach number based on an inlet Mach number and a stagnation temperature ratio. This approach provides a tool for analysing the steady effects of heat transfer on flow characteristics in a quasi-one-dimensional setting. The solution procedure involves discretising the domain of interest into small control volumes and solving for each control volume sequentially. If the another property is to be specified at the inlet such as the complete stagnation state or entropy instead of the Mach number, an iterative approach is required to determine the inlet Mach number. For detailed solution methods, refer to [54].

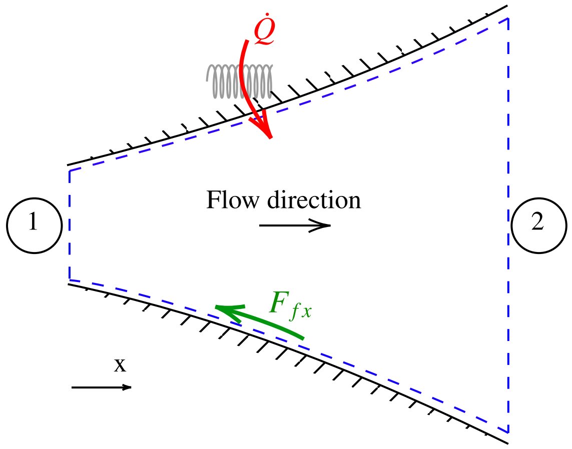

Fig. A.11. Sketch of a control volume with variable area, heat transfer and friction. Dashed lines define the control volume boundary.

We have shown that the Stanton number is a key parameter in the study of heat transfer in compressible flows. The total temperature ratio in Eq. (A.6) can be decomposed further to make the Stanton number appear explicitly.

$$T_{t,2} = T_{t,1} + \frac{Q}{c_p} = T_{t,1} + \mathrm{St}\,A_c\rho_1U_1T_1 = T_{t,1} + \mathrm{St}\,A_c\frac{p_1U_1}{R} \tag{A.7}$$

Where Q is the heat transfer rate, c_p is the specific heat capacity at constant pressure, A_c is the external area, and R is the gas constant.

Aside from this approach, other recent research has expanded to include nonlinear analytical solutions for more generalised cases involving varying area. [52] derived the quasi-one-dimensional linearised Euler equations incorporating heat transfer, subsequently investigating a converging-diverging nozzle with constant heat transfer. Their findings revealed a strong dependence of the nozzle's acoustic and entropy transfer functions on heat transfer. [53] presented a generalised one-dimensional compressible flow analysis, accounting for heat addition and/or friction, for a prescribed pressure-area relation. Furthermore, [51] derived analytical solutions for one-dimensional steady state compressible viscous diabatic flow of an ideal gas through a constant cross-section pipe. While, [25,26] have highlighted limitations in predicting capacity using one-dimensional analysis, the purpose of this approach in our study is to understand the steady state sensitivity of external heat transfer on capacity measurements. The inaccuracies pointed arise from 3D effects or complex flows, but the heat transfer will directly influence the thermodynamic state the flow is in.

Appendix B. Equations for unsteady, quasi-one-dimensional compressible flow with heat transfer (MOC)

The quasi-one-dimensional unsteady Euler equations with heat transfer, expressed in terms of primitive variables, can be written as:

$$\begin{aligned}\frac{\partial\rho}{\partial t} + U\frac{\partial\rho}{\partial x} + \rho\frac{\partial U}{\partial x} &= -\frac{\rho U}{A}\frac{\partial A}{\partial x} && \text{(B.1)}\\ \frac{\partial U}{\partial t} + U\frac{\partial U}{\partial x} + \frac{1}{\rho}\frac{\partial p}{\partial x} &= 0 && \text{(B.2)}\\ \frac{\partial p}{\partial t} + U\frac{\partial p}{\partial x} + \frac{pU\gamma}{A}\frac{\partial A}{\partial x} + p\gamma\frac{\partial U}{\partial x} &= Q\rho U(\gamma-1) && \text{(B.3)}\end{aligned}$$

In matrix form:

$$\frac{\partial\mathbf{Q}}{\partial t} + \mathbf{M}\frac{\partial\mathbf{Q}}{\partial x} = \mathbf{S} \tag{B.4}$$

Where,

$$\mathbf{Q} = \begin{bmatrix}\rho\\ U\\ p\end{bmatrix} \tag{B.5}$$

$$\mathbf{M} = \begin{bmatrix} U & \rho & 0 \\ 0 & U & \frac{1}{\rho} \\ 0 & p\gamma & U \end{bmatrix} = \begin{bmatrix} U & \rho & 0 \\ 0 & U & \frac{1}{\rho} \\ 0 & \rho c^2 & U \end{bmatrix} \tag{B.6}$$

$$\mathbf{S} = \begin{bmatrix} -\frac{\rho U}{A}\frac{\partial A}{\partial x} \\ 0 \\ -\frac{pU}{A}\gamma\frac{\partial A}{\partial x} + Q\rho U(\gamma - 1) \end{bmatrix} \tag{B.7}$$

Decomposing $\mathbf{M}$ in its left and right eigenvectors, one can obtain the compatibility equations for the characteristic variables $\mathbf{W}$.

$$\frac{\partial \mathbf{W}}{\partial t} + \mathbf{\Lambda}\frac{\partial \mathbf{W}}{\partial x} = \mathbf{LS} \tag{B.8}$$

So the compatibility equations become

$$\frac{\partial W_1}{\partial t} = -U \qquad \frac{\partial W_1}{\partial x} \qquad -(\gamma-1)\frac{\rho U}{a^2}\delta Q_x \tag{B.9}$$

$$\frac{\partial W_2}{\partial t} = -(U+a) \qquad \frac{\partial W_2}{\partial x} - Ua\frac{1}{A}\frac{dA}{dx} \qquad +(\gamma-1)\frac{U}{a}\delta Q_x \tag{B.10}$$

$$\frac{\partial W_3}{\partial t} = -(U-a) \qquad \frac{\partial W_3}{\partial x} + Ua\frac{1}{A}\frac{dA}{dx} \qquad -(\gamma-1)\frac{U}{a}\delta Q_x \tag{B.11}$$

To model best the setup of interest, the boundary condition at the inlet should of type total enthalpy-entropy or fixing the stagnation properties. The following development is made under the assumption of no heat flux and constant area at the inlet but can be extended.

$$\partial W_1 = \partial\rho - \frac{1}{a^2}\partial p \tag{B.12}$$

$$\partial W_2 = \partial U + \frac{1}{\rho a}\partial p \tag{B.13}$$

$$\partial W_3 = \partial U - \frac{1}{\rho a}\partial p \tag{B.14}$$

However the variation of entropy is

$$ds = -\frac{\gamma c_v}{\rho}\left(d\rho - \frac{dp}{a^2}\right) \qquad d\rho = -ds\frac{\rho}{\gamma c_v} + \frac{dp}{a^2}$$

Therefore

$$\partial W_1 = \partial\rho - \frac{1}{a^2}\partial p = -\frac{\rho}{\gamma c_v}\partial s \tag{B.15}$$

For the total enthalpy:

$$\begin{aligned} dh_t &= c_p dT + U dU \\ &= c_p T\frac{dT}{T} + U dU \\ &= c_p T\left(\frac{dp}{p} - \frac{d\rho}{\rho}\right) + U dU \\ &= c_p T\left(\frac{\rho a}{2p}(\partial W_2 - \partial W_3) - \partial W_1/\rho - \frac{\rho}{\rho 2a}(\partial W_2 - \partial W_3)\right) \\ &+ U dU \end{aligned} \tag{B.16}$$

$$\begin{aligned} &= c_p T\left((\partial W_2 - \partial W_3)(\frac{\rho a}{2p} - \frac{1}{2a}) - \partial W_1/\rho\right) \\ &+ \frac{u}{2}(\partial W_2 + \partial W_3) \\ &= -\frac{c_p T}{\rho}\partial W_1 + \partial W_2(\frac{\rho a c_p T}{2p} - \frac{c_p T}{2a} + \frac{U}{2}) \\ &+ \partial W_3(-\frac{\rho a c_p T}{2p} + \frac{c_p T}{2a} + \frac{U}{2}) \\ &= -\frac{a^2}{(\gamma-1)\rho}\partial W_1 + \partial W_2(\frac{a c_p}{2R} - \frac{a}{2(\gamma-1)} \\ &+ \frac{U}{2}) + \partial W_3(-\frac{a c_p}{2R} + \frac{a}{2(\gamma-1)} + \frac{U}{2}) \end{aligned} \tag{B.17}$$

A similar expression can be derived for prescribing the stagnation pressure. At the outlet, the static pressure is specified in case of subsonic outflow. To avoid the reflection of the characteristics at the outlet, a non-reflecting boundary condition is used [56].

As one of the focus of this study is the transient behaviour of the flow in transonic nozzles, it is expected that sonic conditions will be encountered. Numerical methods often encounter difficulties when dealing with sonic points. In these cases, a phenomenon known as the sonic glitch may occur. The sonic glitch manifests as a small, non-physical discontinuity or visible error in the computed solution around the sonic point [57]. To ensure a smooth transition as the flow accelerates through the sonic point, an entropy fix is implemented. This approach, as discussed by Va et al. [58], helps preserve the continuity of the solution across the sonic threshold. The entropy fix is particularly crucial in maintaining the accuracy and stability of our numerical simulations as the flow transitions from subsonic to supersonic regimes.

Data availability

Data will be made available on request.

References

[1] S. Sharma, M. Shadloo, A. Hadjadj, Turbulent flow topology in supersonic boundary layer with wall heat transfer, Int. J. Heat Fluid Flow 78 (2019) 108430, http://dx.doi.org/10.1016/j.ijheatfluidflow.2019.108430, URL: https://www.sciencedirect.com/science/article/pii/S0142727X18306027.

[2] S.U. Choi, J.A. Eastman, Enhancing thermal conductivity of fluids with nanoparticles, 1995, URL: https://www.osti.gov/biblio/196525.

[3] M.T. Lewis, J.-P. Hickey, Conjugate heat transfer in high-speed external flows: A review, J. Thermophys. Heat Transfer 37 (2023) 697–712, http://dx.doi.org/10.2514/1.T6763.

[4] B. John, P. Senthilkumar, S. Sadasivan, Applied and theoretical aspects of conjugate heat transfer analysis: A review, Arch. Comput. Methods Eng. 2 (2018) 475–489.

[5] T. Tu, S. Chen, C. Xu, Conjugated heat transfer simulation of flow mechanism and heat transfer characteristic of sweeping jet impinging on leading edge in turbine cascade, Appl. Therm. Eng. 236 (2024) 121839, http://dx.doi.org/10.1016/j.applthermaleng.2023.121839, URL: https://www.sciencedirect.com/science/article/pii/S1359431123018689.

[6] Q. He, W. Zhao, Z. Chi, S. Zang, Application of deep-learning method in the conjugate heat transfer optimization of full-coverage film cooling on turbine vanes, Int. J. Heat Mass Transfer 195 (2022) 123148.

[7] E.C. Okafor, M. Tsukamoto, A. Hayakawa, K.K.A. Somarathne, T. Kudo, T. Tsujimura, H. Kobayashi, Influence of wall heat loss on the emission characteristics of premixed ammonia-air swirling flames interacting with the combustor wall, Proc. Combust. Inst. 38 (2021) 5139–5146, http://dx.doi.org/10.1016/j.proci.2020.06.142, URL: https://www.sciencedirect.com/science/article/pii/S1540748920302224.

[8] S. Gövert, D. Mira, J.B.W. Kok, M. Vázquez, G. Houzeaux, The effect of partial premixing and heat loss on the reacting flow field prediction of a swirl stabilized gas turbine model combustor, Flow Turbul. Combust. 100 (2018) 503–534, http://dx.doi.org/10.1007/s10494-017-9848-4.

[9] D. Bruna, M.G. Turner, Isothermal boundary condition at casing applied to the rotor 37 transonic axial flow compressor, J. Turbomach. 135 (2013) 034501, http://dx.doi.org/10.1115/1.4007569.

[10] K.P. Griffin, L. Fu, P. Moin, Velocity transformation for compressible wall-bounded turbulent flows with and without heat transfer, Proc. Natl. Acad. Sci. 118 (2021) e2111144118, http://dx.doi.org/10.1073/pnas.2111144118, URL: https://www.pnas.org/doi/abs/10.1073/pnas.2111144118.

[11] M. Lazareff, R. Moretti, M.-P. Errera, Coupling methodology for thermal fluid-solid simulations through a full transient flight cycle, Int. J. Heat Mass Transfer 202 (2023) 123691, http://dx.doi.org/10.1016/j.ijheatmasstransfer.2022.123691, URL: https://www.sciencedirect.com/science/article/pii/S0017931022011590.

[12] M. Fiore, V. Barbato, F. Nasuti, Transient analysis of liquid rocket engine chilldown and startup by conjugate heat transfer approach, 2024, http://dx.doi.org/10.2514/6.2024-0353, URL: https://arc.aiaa.org/doi/abs/10.2514/6.2024-0353.

[13] P. Wang, F. Li, S. Xu, Y. Liu, Transient thermal behaviors of ultra-supercritical steam turbine control valves during the cold start warm-up process: Conjugate heat transfer simulation and field data validation, J. Heat Transf. 141 (2019) 122901, http://dx.doi.org/10.1115/1.4044834.

[14] J.R. Edwards, J.A. Boles, R.A. Baurle, Large-eddy/reynolds-averaged navier–stokes simulation of a supersonic reacting wall jet, Combust. Flame 159 (2012) 1127–1138, http://dx.doi.org/10.1016/j.combustflame.2011.10.009, URL: https://www.sciencedirect.com/science/article/pii/S0010218011003142.

[15] J. Muller, C. Johnson, M. Dutta, J.C. Oefelein, Analysis of shock-wave/boundary-layer interaction unsteadiness mechanisms using conjugate heat transfer and wall-modeled les, 2025, http://dx.doi.org/10.2514/6.2025-1892, URL: https://arc.aiaa.org/doi/abs/10.2514/6.2025-1892, http://arxiv.org/abs/https://arc.aiaa.org/doi/pdf/10.2514/6.2025-1892arXiv:https://arc.aiaa.org/doi/pdf/10.2514/6.2025-1892.

[16] M.G. Adams, T. Povey, B.F. Hall, D.N. Cardwell, K.S. Chana, P.F. Beard, Commissioning of a combined hot-streak and swirl profile generator in a transonic turbine test facility, J. Eng. Gas Turbines Power 142 (2020) 031008, http://dx.doi.org/10.1115/1.4044224.

[17] J. Amend, R. Lubbock, F. Ornano, T. Povey, Lean-burn combustor simulator for an engine-component test facility: An experimental and computational study, J. Turbomach. 145 (2023) 061014, http://dx.doi.org/10.1115/1.4056387.

[18] S.T. Englerth, An experimental conduction error calibration procedure for cooled total temperature probes, 2015, URL: https://api.semanticscholar.org/CorpusID:102301762.

[19] D. Bianchi, A. Turchi, F. Nasuti, M. Onofri, Coupled cfd analysis of thermochemical erosion and unsteady heat conduction in solid rocket nozzles, in: 48th AIAA/ASME/SAE/ASEE Joint Propulsion Conference & Exhibit, 2012, p. 4318.

[20] S. Xue, A. Roy, W.F. Ng, S.V. Ekkad, A novel transient technique to determine recovery temperature, heat transfer coefficient, and film cooling effectiveness simultaneously in a transonic turbine cascade, J. Therm. Sci. Eng. Appl. 7 (2015) 011016, http://dx.doi.org/10.1115/1.4029098.

[21] D.L. Schultz, Heat transfer measurements in short-duration hypersonic facilities, in: AGARD 165, 1973.

[22] L. He, M. Oldfield, Unsteady conjugate heat transfer modeling, J. Turbomach. 133 (2011).

[23] Analysis of high pressure turbine nozzle guide vanes considering geometric variations, in: Volume 2C: Turbomachinery of *Turbo Expo: Power for Land, Sea, and Air*, 2016, http://dx.doi.org/10.1115/GT2016-57502.

[24] T. Povey, Effect of film cooling on turbine capacity, J. Eng. Gas Turbines Power 132 (2009) 011901, http://dx.doi.org/10.1115/1.3026564.

[25] L. Fielding, The effect of irreversibility on the capacity of a turbine blade row, Proc. Inst. Mech. Eng. 195 (1981) 127–137.

[26] I.V. Afanasiev, A.V. Granovski, A.M. Kareline, M.K. Kostege, The problems of inaccuracy in flow capacity definition by using different numerical techniques, J. Therm. Sci. 13 (2004) 1–7, http://dx.doi.org/10.1007/s11630-004-0001-z.

[27] D. Burdett, C. Hambidge, T. Povey, Analysis of ultra-low uncertainty gas turbine flow capacity measurement techniques, Proc. Inst. Mech. Eng. Part A: J. Power Energy 235 (2021) 1053–1079, http://dx.doi.org/10.1177/0957650920909718.

[28] C. Hirsch, Numerical Computation of Internal and External Flows: The Fundamentals of Computational Fluid Dynamics, Elsevier, 2007.

[29] R.A. Delaney, P. Kavanagh, Transonic flow analysis in axial-flow turbomachinery cascades by a time-dependent method of characteristics, J. Eng. Power 98 (1976) 356–363, http://dx.doi.org/10.1115/1.3446181.

[30] M.J. Zucrow, J.D. Hoffman, Gas dynamics, in: Multidimensional Flow, Vol. 2, New York, 1977.

[31] R.I. Issa, D.B. Spalding, Unsteady one-dimensional compressible frictional flow with heat transfer, J. Mech. Eng. Sci. 14 (1972) 365–369.

[32] Y.M. Huang, Study of unsteady flow in a heat exchanger by the method of characteristics, J. Press. Vessel. Technol. 114 (1992) 459–463, http://dx.doi.org/10.1115/1.2929255.

[33] Y. Dreze, M. Hao, L. di Mare, Divergence-free turbulent inflow data from realistic covariance tensor, Phys. Fluids 35 (2023) 025120, http://dx.doi.org/10.1063/5.0136568.

[34] J. Hope-Collins, L. di Mare, Artificial diffusion for convective and acoustic low mach number flows i: Analysis of the modified equations, and application to roe-type schemes, J. Comput. Phys. 475 (2023) 111858, http://dx.doi.org/10.1016/j.jcp.2022.111858, URL: https://www.sciencedirect.com/science/article/pii/S0021999122009214.

[35] M. Hao, J. Hope-Collins, L. di Mare, Generation of turbulent inflow data from realistic approximations of the covariance tensor, Phys. Fluids 34 (2022) http://dx.doi.org/10.1063/5.0106664.

[36] M. Hao, L. di Mare, Budgets of reynolds stresses in film cooling with fan-shaped and cylindrical holes, Phys. Fluids 35 (2023) http://dx.doi.org/10.1063/5.0140670.

[37] M. Čada, M. Torrilhon, Compact third-order limiter functions for finite volume methods, J. Comput. Phys. 228 (2009) 4118–4145, http://dx.doi.org/10.1016/j.jcp.2009.02.020, URL: https://www.sciencedirect.com/science/article/pii/S0021999109000953.

[38] A.H. Shapiro, The dynamics and thermodynamics of compressible fluid flow, 1953.

[39] H. Kawamura, K. Ohsaka, H. Abe, K. Yamamoto, Dns of turbulent heat transfer in channel flow with low to medium-high prandtl number fluid, Int. J. Heat Fluid Flow 19 (1998) 482–491, http://dx.doi.org/10.1016/S0142-727X(98)10026-7, URL: https://www.sciencedirect.com/science/article/pii/S0142727X98100267.

[40] S. Pirozzoli, D. Modesti, P. Orlandi, F. Grasso, Turbulence and secondary motions in square duct flow, J. Fluid Mech. 840 (2018) 631–655, http://dx.doi.org/10.1017/jfm.2018.66.

[41] J.C. Sivells, Aerodynamic design of axisymmetric hypersonic wind-tunnel nozzles, J. Spacecr. Rockets 7 (1970) 1292–1299, http://dx.doi.org/10.2514/3.30160.

[42] J.C. Sivells, R.G. Payne, A Method of Calculating Turbulent-Boundary-Layer Growth at Hypersonic Mach Numbers, Vol. 59, Arnold Engineering Development Center, Air Research and Development Command …, 1959.

[43] L. Back, P. Massier, H. Gier, Convective heat transfer in a convergent-divergent nozzle, Int. J. Heat Mass Transfer 7 (1964) 549–568, http://dx.doi.org/10.1016/0017-9310(64)90052-3, URL: https://www.sciencedirect.com/science/article/pii/0017931064900523.

[44] A.H.K. Bensayah, A. Bounif, Heat transfer in turbulent boundary layers of conical and bell shaped rocket nozzles with complex wall temperature, Numer. Heat Transf. Part A: Appl. 66 (2014) 289–314, http://dx.doi.org/10.1080/10407782.2013.873283.

[45] A. Makhija, K. Bodi, D. Chakraborty, Numerical estimation of convective heat transfer coefficient and heat flux for a supersonic rocket nozzle, Def. Sci. J. 74 (2024) 189–196, http://dx.doi.org/10.14429/dsj.74.19633.

[46] E. Zhalehrajabi, N. Rahmanian, N. Hasan, Effects of mesh grid and turbulence models on heat transfer coefficient in a convergent–divergent nozzle, Asia-Pac. J. Chem. Eng. 9 (2014) 265–271, http://dx.doi.org/10.1002/apj.1767, URL: https://onlinelibrary.wiley.com/doi/abs/10.1002/apj.1767, http://arxiv.org/abs/https://onlinelibrary.wiley.com/doi/pdf/10.1002/apj.1767arXiv:https://onlinelibrary.wiley.com/doi/pdf/10.1002/apj.1767.

[47] J.D. Wright, W. Kang, A.N. Johnson, V.B. Khromchenko, M.R. Moldover, L. Zhang, B. Mickan, Thermal boundary layers in critical flow venturis, Flow Meas. Instrum. 81 (2021) 102025, http://dx.doi.org/10.1016/j.flowmeasinst.2021.102025, URL: https://www.sciencedirect.com/science/article/pii/S095559862100131X.

[48] C. Wang, G. Wang, H. Ding, Thermal effect on body temperature distribution of the critical flow venturi nozzle, Exp. Therm. Fluid Sci. 79 (2016) 187–194, http://dx.doi.org/10.1016/j.expthermflusci.2016.07.012, URL: https://www.sciencedirect.com/science/article/pii/S0894177716301844.

[49] H. Ding, C. Wang, G. Wang, Transient conjugate heat transfer in critical flow nozzles, Int. J. Heat Mass Transfer 104 (2017) 930–942, http://dx.doi.org/10.1016/j.ijheatmasstransfer.2016.09.021, URL: https://www.sciencedirect.com/science/article/pii/S0017931016314065.

[50] Mitsuharu Masuda Kazuyasu Matsuo Yutaka Yamaguchi Miyazato, Masashi Kashitani, One—dimensional analysis of thermal choking in case of heat addition in ducts, 2000, URL: https://api.semanticscholar.org/CorpusID:108846797.

[51] A. Ferrari, Analytical solutions for one-dimensional diabatic flows with wall friction, J. Fluid Mech. 918 (2021) A32, http://dx.doi.org/10.1017/jfm.2021.278.

[52] S.R. Yeddula, J. Guzmán-Iñigo, A.S. Morgans, A solution for the quasi-one-dimensional linearised euler equations with heat transfer, J. Fluid Mech. 936 (2022) R3, http://dx.doi.org/10.1017/jfm.2022.101.

[53] W. Loh, A generalized one-dimensional compressible flow analysis with heat addition and/or friction in a non-constant area duct, Internat. J. Engrg. Sci. 8 (1970) 193–206, http://dx.doi.org/10.1016/0020-7225(70)90030-3, URL: https://www.sciencedirect.com/science/article/pii/0020722570900303.

[54] A.A. Oliva, S.C. Morris, Steady, quasi-one-dimensional, internal compressible flow with area change, heat addition and friction, J. Fluid Mech. 957 (2023) A15, http://dx.doi.org/10.1017/jfm.2023.44.

[55] M.J. Rahimi, H.K. Chelliah, Simplified approach to identify thermal choking limits of a dual-mode variable area combustor, AIAA J. 56 (2018) 2091–2095, http://dx.doi.org/10.2514/1.J055848.

[56] T. Poinsot, S. Lelef, Boundary conditions for direct simulations of compressible viscous flows, J. Comput. Phys. 101 (1992) 104–129, http://dx.doi.org/10.1016/0021-9991(92)90046-2.

[57] H. Tang, On the sonic point glitch, J. Comput. Phys. 202 (2005) 507–532, http://dx.doi.org/10.1016/j.jcp.2004.07.013, URL: https://www.sciencedirect.com/science/article/pii/S0021999104002967.

[58] B. Va, W.-T. Lee, K. Powell, Sonic-point capturing, 1989, http://dx.doi.org/10.2514/6.1989-1945, URL: https://arc.aiaa.org/doi/abs/10.2514/6.1989-1945.